

# Observations of High-Energy Gamma-Ray Emission Toward the Galactic Centre with the *Fermi* Large Area Telescope

---

**Troy A. Porter<sup>\*a</sup> and Simona Murgia<sup>b</sup> on behalf of the *Fermi*-LAT Collaboration**

<sup>a</sup>*Hansen Experimental Physics Laboratory and Kavli Institute for Particle Astrophysics and Cosmology, Stanford University, Stanford, CA 94305, U.S.A.*

<sup>b</sup>*Department of Physics and Astronomy, University of California, Irvine, CA 92697, U.S.A.*

*E-mail:* [tporter@stanford.edu](mailto:tporter@stanford.edu), [smurgia@uci.edu](mailto:smurgia@uci.edu)

The inner region of the Milky Way is one of the most interesting and complex regions of the  $\gamma$ -ray sky. The intense interstellar emission and resolved point sources, as well as potential contributions by other sources such as unresolved source populations and dark matter, complicate the interpretation of the data. In this contribution the *Fermi*-LAT team analysis of a  $15^\circ \times 15^\circ$  region about the Galactic centre is described. The methodology for point-source detection and treatment of the interstellar emission is given. In general, the bulk of the  $\gamma$ -ray emission from this region is attributable to a combination of these two contributions. However, low-intensity residual emission remains and its characterisation is discussed.

*The 34th International Cosmic Ray Conference,  
30 July- 6 August, 2015  
The Hague, The Netherlands*

---

\*Speaker.

## 1. Introduction

The region surrounding the Galactic centre (GC) is among the brightest and most complex in high-energy  $\gamma$ -rays, with on-going massive star formation providing all types of known or suspected cosmic ray (CR) and  $\gamma$ -ray sources. The GC also houses a  $\sim 10^6 M_{\odot}$  black hole (e.g., [1]) and the region is predicted to be the brightest source of  $\gamma$ -rays associated with annihilation or decay of massive weakly-interacting particles (see the reviews by, e.g., [2, 3, 4]). Despite detection in the 100 MeV to GeV range by the EGRET instrument on the *Compton Gamma-Ray Observatory* [5] and at higher energies by the H.E.S.S. Cherenkov array [6, 7] the characterisation of the  $\gamma$ -ray emission for  $< 100$  GeV energies in the region surrounding the GC has remained elusive.

The  $\gamma$ -ray emission in the Galaxy is predominantly due to the interactions of CR particles with the interstellar gas and radiation fields. This interstellar emission is a fore-/background against which  $\gamma$ -ray point sources are detected. In the Galactic plane, and particularly toward the GC, the intensity of this emission makes disentangling the contributions by  $\gamma$ -ray point sources and truly diffuse processes particularly challenging.

Since 2008 the Large Area Telescope instrument on the *Fermi* Gamma-Ray Space Telescope (*Fermi*-LAT) has been taking data in the range 20 MeV to more than 300 GeV energies. In this contribution, an analysis is described of the  $\gamma$ -ray emission observed by the *Fermi*-LAT during the first 62 months of the mission toward the inner Milky Way that characterises the  $15^{\circ} \times 15^{\circ}$  region in Galactic coordinates centred on the GC. This encompasses the innermost  $\sim 1$  kpc where the CR intensities, interstellar gas and radiation field densities are highest but most uncertain, and signatures of new physics may be detectable. The analysis uses multiple interstellar emission models (IEMs) together with an iterative fitting procedure to self-consistently determine the contributions by diffuse and discrete sources of high-energy  $\gamma$ -ray emission. The *GALPROP* CR propagation code<sup>1</sup> (e.g., [8, 9]) is used to calculate components of IEMs that are fit to the *Fermi*-LAT data to predict the interstellar emission fore-/background toward the  $15^{\circ} \times 15^{\circ}$  region. Candidate locations of point sources are found using a wavelet-based algorithm [10, 11]. These are used together with the IEMs to define a model for the emission of the region, which is then optimised in a maximum-likelihood fit to determine the contribution by CR-induced diffuse emission from the innermost  $\sim 1$  kpc and  $\gamma$ -ray point sources.

## 2. Methodology

### 2.1 Data Selection and Preparation

The analysis employs events with reconstructed energy in the range 1–100 GeV, where the effective area of the LAT is largest and not strongly dependent on energy. To allow the best separation between point sources and the structured interstellar emission in the analysis procedure, only front-converting events are used.

Events are selected from approximately 62 months of data from 2008-08-11 until 2013-10-15 using the standard low-residual CR background “Clean” events from the Pass 7 event selections<sup>2</sup>.

<sup>1</sup>For a detailed description of the *GALPROP* code the reader is referred to the dedicated website: <http://galprop.stanford.edu>

<sup>2</sup>The reprocessed data and instrument response functions P7REP\_CLEAN\_V15 are employed.

Exposure maps and the PSF for the pointing history of the observations were generated using the standard *Fermi*-LAT ScienceTools package (version 09-34-02) available from the *Fermi* Science Support Center<sup>3</sup>.

## 2.2 Fore-/Background Modelling

Specialised IEMs are constructed to estimate the fore-/background interstellar emission toward and through the  $15^\circ \times 15^\circ$  region about the GC. The results of the *Fermi*-LAT team study [12], which compared *GALPROP*-generated IEMs normalised to local CR measurements with  $\gamma$ -ray data, are used. A major uncertainty affecting predictions of the interstellar emission toward the inner Galaxy is the spatial distribution of CR sources. The pulsar distribution (“Pulsars” [15]) and the distribution of OB stars (“OBstars” [16]) employed in the aforementioned *Fermi*-LAT study encapsulate this because they represent reasonable extremes for the Galactocentric radial dependence<sup>4</sup>. These CR source distributions are used<sup>5</sup> to calculate “baseline”  $\gamma$ -ray intensity templates for Galactocentric radial annuli for the standard processes ( $\pi^0$ -decay, IC, Bremsstrahlung<sup>6</sup>). The annular intensity maps are used as templates together with an isotropic component and a model for  $\gamma$ -ray emission associated with the Loop I supernova remnant (SNR) employing a two-component spatial template from [13] with a power-law spectral model for each, and point sources from the Third Fermi source catalogue (3FGL; [14]). The combined model for each IEM is fit to the *Fermi*-LAT data *excluding the  $15^\circ \times 15^\circ$  region about the GC* using a maximum-likelihood method.

Figure 1 shows the fractional residuals,  $(data - model)/model$ , for the Pulsars IEM for the 1–3.16 GeV energy band for the (left to right) baseline, and two IEM variants of this model that have been scaled to the data (described below). The regions not used in the fitting procedure are explicitly masked in the figure. They are not used because of localised extended excesses that are most likely unrelated to the large-scale interstellar emission.

Outside of the Galactic plane the fractional residuals are substantially reduced for the IEM shown in the central panel compared to the baseline. This IEM variant is termed ‘intensity-scaled’ because only the normalisations of the individual intensity maps are adjusted in the scaling procedure. The lower residuals for this IEM are due to the scaling of the  $\pi^0$ -decay interstellar emission for the local annulus, and of the IC component generally. Along the Galactic plane the  $\gtrsim 30\%$  under-prediction by the baseline model is reduced to  $\lesssim \pm 10\%$  after this scaling, except for scattered regions. However, at higher energies (not shown) the intensity-scaled IEM tends to over-predict the data along the plane interior to the solar circle. To account for this, another variant is developed that includes additional degrees of freedom to the spectrum of the  $\pi^0$ -decay emission for annuli interior to the solar circle. It is fit to the data following the same procedure as the intensity-scaled IEM. This variant is termed ‘index-scaled’ and has a fractional residual  $\lesssim \pm 10\%$  for longitudes  $l \sim -(15 - 70)^\circ$  for the 1–3.16 GeV band (Fig. 1, right panel), with a slight increase in the residual

<sup>3</sup><http://fermi.gsfc.nasa.gov/ssc/data/analysis/>

<sup>4</sup>The reader is referred to Fig. 1 in [12] for a visualisation of the Galactocentric radial variation.

<sup>5</sup>The models assume an axisymmetric cylindrical geometry for the CR confinement volume with a halo height  $z_h = 6$  kpc and maximum radial boundary  $R_h = 30$  kpc, and all other parameters the same so that the only difference is the assumed spatial distribution for the CR sources.

<sup>6</sup>Bremsstrahlung is a minor component over the 1–100 GeV energy range used in the analysis, and is held constant at the *GALPROP* predictions for each IEM.

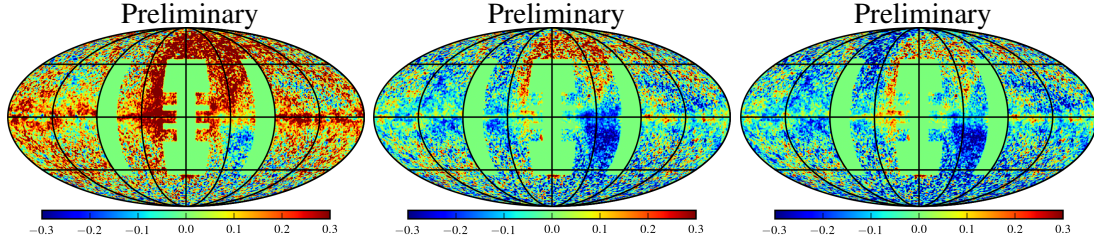


**Figure 1:** Residual fractional counts  $(data - model)/model$  in the 1–3.16 GeV energy range for the baseline Pulsars model (left), intensity-scaled Pulsars model (centre), and index-scaled Pulsars model (right) fitted following the procedure described in the text. The baseline model does not include a model for the Loop-I SNR, resulting in the positive residuals in the northern Galactic hemisphere inside the solar circle. The maps are calculated for a HEALPix [17] order 8 pixelisation ( $\sim 0.23^\circ$  resolution) and smoothed with a  $1^\circ$  FWHM Gaussian. The positive residual at mid-to-high latitudes interior to the solar circle is due to mismatch between the data and the relatively simple Loop I model. The residuals close to the plane caused by this simple model are lower and do not affect the analysis of the  $15^\circ \times 15^\circ$  region about the GC.

for the corresponding positive longitude range; the residuals improve to a similar degree at higher energies. Qualitatively, similar results for the scaled OBstars IEMs (intensity/index-scaled) are also obtained. It is not straightforward to identify a best IEM after fitting because the qualitative improvement for each over the corresponding baseline IEM is similar. Consequently all 4 IEMs are used to estimate the fore-/background below.

### 2.3 Modelling $15^\circ \times 15^\circ$ Region about the Galactic Centre

Modelling of the interstellar emission and point sources over the  $15^\circ \times 15^\circ$  region about the GC is accomplished using an iterative procedure that identifies point-candidates (‘seeds’) and fits for their fluxes and spectra together with the interstellar emission from  $\pi^0$ -decay associated with the neutral gas and IC components for the innermost annulus using a maximum-likelihood method, while the fore-/background interstellar emission (determined above) outside the inner  $\sim 1$  kpc is held constant.

Point-source seeds are identified using the wavelet analysis algorithm *PGWave* [10, 11]. Application of *PGWave* identifies true point sources, as well as structures in the interstellar emission that are indistinguishable from point sources due to the finite angular resolution and statistics of the *Fermi*-LAT data, without dependence on the specifics of an IEM. The spectra of candidates are initially evaluated using *PointLike*, a package for maximum-likelihood analysis of *Fermi*-LAT data [18, 19]. This package is also used to optimise the positions of seeds from the *PGWave*-determined list. For the only extended source that has been previously identified in the region, the W28 supernova remnant [20], the spatial template and spectral model employed for the 3FGL analysis are used. Its spectral parameters are refit during the maximum-likelihood procedure.

Point-source candidates are combined with their *PointLike* trial spectra together with the fore-/background models in a second maximum-likelihood fit. A binned likelihood fit is performed using the *Fermi* ScienceTool *glike*. The templates for the  $\pi^0$ -decay related  $\gamma$ -ray intensity from H I and CO, and the IC emission, in annulus 1 are freely scaled in the fitting procedure. The point-source seed detection is run again on the residual maps to find fainter sources that were missed in the first iteration. *PointLike* is again used to determine their initial spectra and optimise

their localisations. The combined point-source candidate list from the first and second iterations<sup>7</sup>, and the interstellar emission components for annulus 1 are fit using *gtlike*. The results of the maximum-likelihood fit are values and confidence ranges for the coefficients of the H I annulus 1, CO annulus 1, IC annulus 1, as well as the  $TS$ , fluxes and spectra for the point sources. All point sources with a maximum-likelihood determined  $TS > 9$  are included in the model.

### 3. Results

#### 3.1 Interstellar Emission

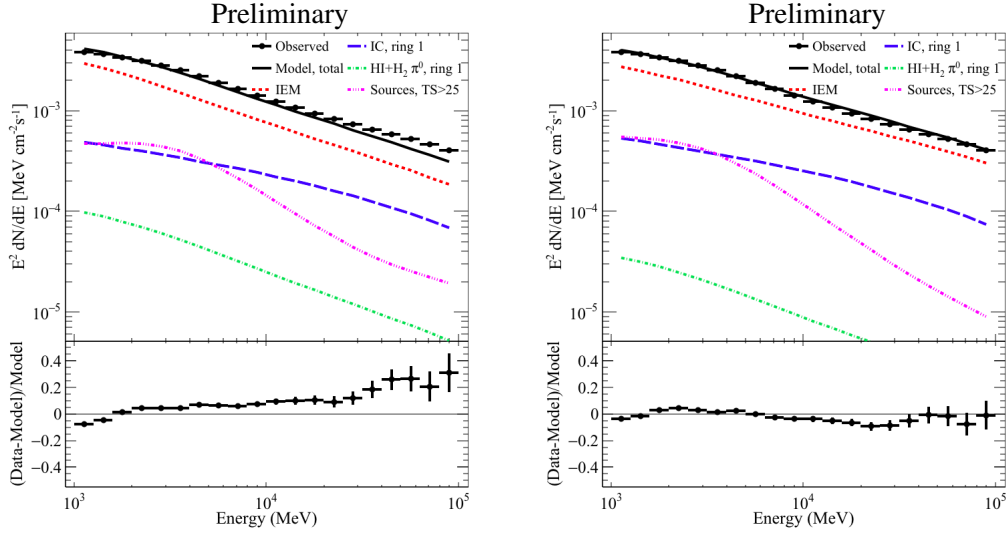


**Figure 2:** Differential flux components obtained for the Pulsars intensity-scaled (left) and index-scaled (right) IEMs for the  $15^\circ \times 15^\circ$  region about the GC. Line styles, as in figure legend. Solid circles: data.

Figure 2 shows the differential spectra of the individual components obtained for the Pulsars intensity-scaled and index-scaled IEMs integrated over the  $15^\circ \times 15^\circ$  region about the GC (the results for the OB stars IEMs are similar, but not shown due to space limitations). The figure separates the emission components in terms of the contributions by  $\pi^0$ -decay and IC for annulus 1, the interstellar emission fore-/background, and point sources over the region. As expected, the fore-/background dominates for each IEM, which is predominantly  $\pi^0$ -decay in origin. Interestingly, the IC is the dominant interstellar emission component over the inner  $\sim 1.5$  kpc, and is much higher than predicted by *GALPROP* for the baseline IEMs. Its contribution to the total flux depends on the IEM and whether the residual is fitted (Section 3.3). The variation of the IC flux for annulus 1 over all 4 IEMs is within a factor  $\sim 1.5$ . The interstellar emission from the neutral gas  $\pi^0$ -decay is considerably suppressed compared to the *GALPROP* predictions. For both Pulsars and OBstars models the interstellar emission fore-/background is harder at high energies for the index-scaled IEMs, which reduces the spectral residuals for energies  $\gtrsim 10$  GeV.

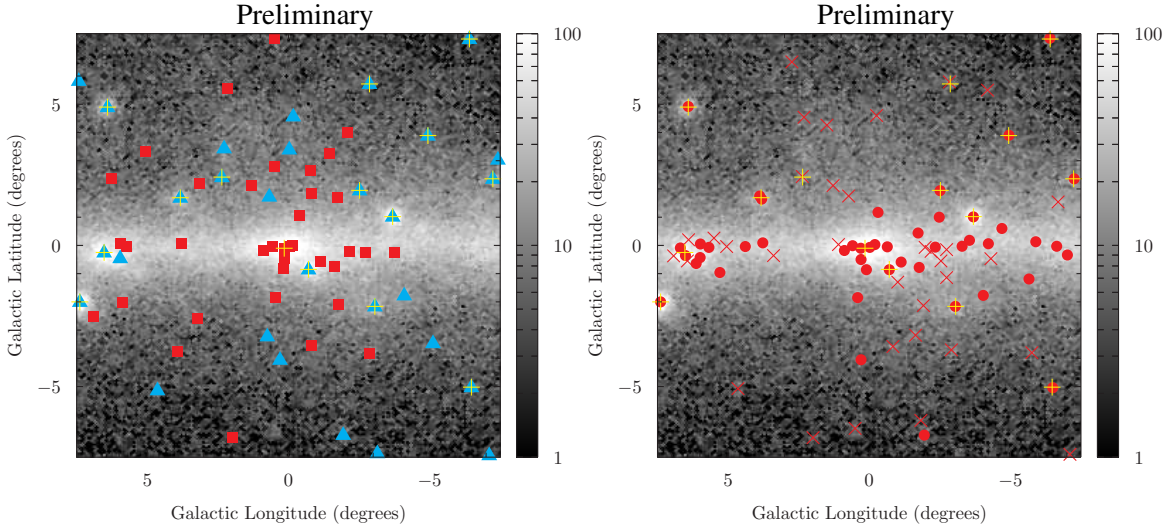


**Figure 3:** Point sources for 3FGL (left panel) and 1FIG (right panel, for Pulsars intensity-scaled IEM) overlaid on the total counts for the  $15^\circ \times 15^\circ$  region about the GC. Left panel symbol key: filled squares, ‘flagged’ 3FGL sources; filled triangles, other 3FGL sources; upright crosses, 3FGL sources with a multi-wavelength association. Right panel symbol key: filled circles, 1FIG sources with  $TS \geq 25$ ; angled crosses, 1FIG source candidates with  $TS < 25$ ; upright crosses, as in left panel. Colour scale is in counts per  $0.05^2$  degree pixel.

### 3.2 Point Sources

The analysis finds 48 point sources over the  $15^\circ \times 15^\circ$  region about the GC with a  $TS \geq 25$  for the Pulsars intensity-scaled IEM, which was the model used for the point-source positions and localisation uncertainties<sup>8</sup>. This collection is denoted the 1<sup>st</sup> Fermi Inner Galaxy (1FIG) source list. Figure 3 shows the point sources from the 3FGL and 1FIG overlaid on the total photon counts for the  $15^\circ \times 15^\circ$  region about the GC. The 3FGL sources are separated according to whether they have an analysis flag set in the 3FGL catalogue: flagged sources indicate their properties depend on the IEM or other details of the analysis in the region. The density of flagged 3FGL sources is higher out of the Galactic plane than that of the 1FIG sources, even if the  $TS < 25$  source candidates are included. This can be partly attributed to differences in the IEMs used for the respective analyses.

Some of the 1FIG sources and source candidates are likely due to mismodelling of the interstellar emission. However, it is difficult to determine the precise fraction. Multi-wavelength association with objects of known  $\gamma$ -ray emitting source classes can suggest counterparts. There are 14 1FIG source and source candidate overlaps when comparing with SNRs from Green’s SNR catalogue<sup>9</sup> [21] and pulsars from the ATNF catalogue<sup>10</sup> [22]. Multiple overlaps occur across and within the catalogues, e.g., SNR 354.1+00.1 and PSR J1701-3006A,D,E overlap with 1FIG J1701.1-3004. Three of the 1FIG sources overlap with SNRs that have not previously been detected in high-energy  $\gamma$ -rays; follow-on studies are required to better characterise their spatial and spectral properties.

<sup>7</sup>No new significant excesses that could be identified as viable seeds were found after two iterations of the procedure.

<sup>8</sup>The optimisation of the source seed localisation does not have a strong dependence on the IEM.

<sup>9</sup><http://www.mrao.cam.ac.uk/surveys/snrs/>

<sup>10</sup><http://www.atnf.csiro.au/people/pulsar/psrcat/>

### 3.3 Residuals

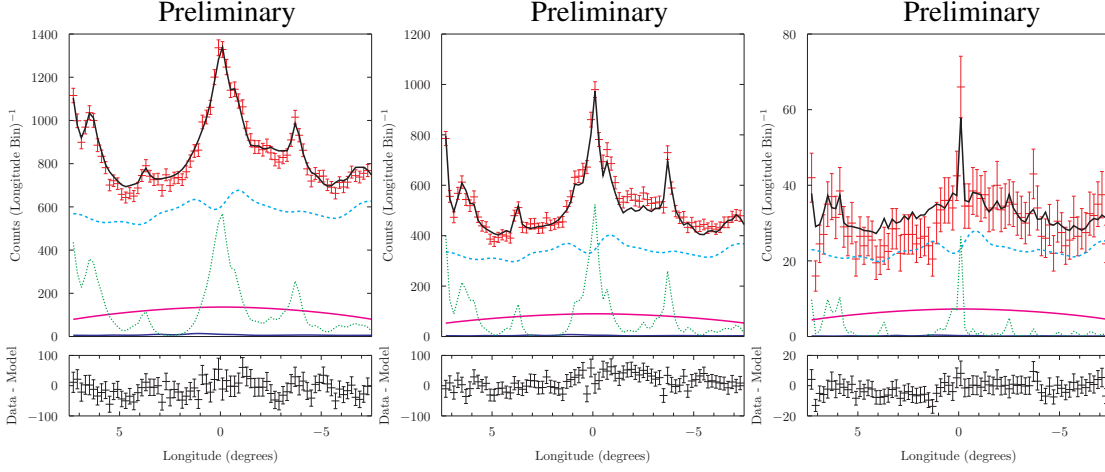


**Figure 4:** Longitude profiles for 1–1.6 (left), 1.6–10 (middle), and 10–100 GeV energies (left), respectively, of the residual counts,  $data - model$ , for the Pulsars index-scaled IEM after fitting for interstellar emission and point sources across the  $15^\circ \times 15^\circ$  region. Line styles: black/solid, total model; cyan/dashed, fore/background interstellar emission; green/dotted, point sources; magenta/solid, IC from annulus 1; blue/solid,  $\pi^0$ -decay from annulus 1. Point styles: red, data; black, residual counts. The lower sub-panel for each profile gives the residual counts after the model has been subtracted from the data. The error bars are statistical. Profiles for the residuals counts for other IEMs display similar features with the major difference being the number of counts.

Figure 4 shows the longitude profiles for the 1–1.6, 1.6–10, and  $> 10$  GeV energy ranges<sup>11</sup> for the Pulsars index-scaled model, which is the model that has the lowest fractional residual across the 1–100 GeV energy range. The lower sub-panel for each figure gives the residual counts,  $data - model$ . (The features are mostly the same for the other IEMs.) While there is considerable statistical noise, there is some indication that the residual counts are distributed asymmetrically in longitude about the GC below 10 GeV.

The model over prediction at the lowest energies is primarily correlated with the Galactic plane, which could be due to mismodelling of the gas component of the IEMs. Some of the positive residual in the few GeV range could be due to an extended component that is more concentrated toward the GC compared to the IEM components. However, it is difficult to establish properties for an additional component not presently included in the model for the region. Different spatial models are considered for the positive residuals: a squared Navarro-Frenk-White (NFW) profile [23] for dark matter annihilation, 2D Gaussians with HWHM  $1^\circ$ ,  $2^\circ$ ,  $5^\circ$ , and  $10^\circ$ , and the CO annulus 1 gas template smoothed with a  $2^\circ$  Gaussian as a tracer of unresolved pulsars. An exponential cutoff power law is used for the spectral model, which has some flexibility to model a pulsar or a DM annihilation spectrum without supposing specific scenarios. The positive residual model is fit together with the interstellar emission and point sources (Sec. 2.3). Its flux and spectral parameters depend strongly on the interstellar emission fore-/background, and are also covariant with the normalisations of the standard interstellar emission processes ( $\pi^0$ -decay and IC) for annulus 1. Note

<sup>11</sup>Each band covers the energy intervals where the under/over-predictions for the fractional residuals are more prominent in Fig. 2.

that not all of the positive residual is accounted for by the centrally peaked models that are considered here. The remainder is distributed about the Galactic plane, but with no obvious correlation to the spatial templates used for the analysis.

## Acknowledgments

The *Fermi*-LAT Collaboration acknowledges support for LAT development, operation and data analysis from NASA and DOE (United States), CEA/Irfu and IN2P3/CNRS (France), ASI and INFN (Italy), MEXT, KEK, and JAXA (Japan), and the K.A. Wallenberg Foundation, the Swedish Research Council and the National Space Board (Sweden). Science analysis support in the operations phase from INAF (Italy) and CNES (France) is also gratefully acknowledged.

GALPROP development is partially funded via NASA grants NNX10AE78G and NNX13AC47G.

SM's work is supported by a fellowship from the Hellman Foundation and the US DOE.

## References

- [1] Genzel, R., Eisenhauer, F., & Gillessen, S. 2010, *Reviews of Modern Physics*, 82, 3121
- [2] Jungman, G., Kamionkowski, M., & Griest, K. 1996, *Physics Reports*, 267, 195
- [3] Bergström, L. 2000, *Reports on Progress in Physics*, 63, 793
- [4] Feng, J. L. 2010, *Ann. Rev. Astron. & Astrophys.*, 48, 495
- [5] Mayer-Hasselwander, H. A., et al. 1998, *A&A*, 335, 161
- [6] Aharonian, F., et al. 2006, *Nature*, 439, 695
- [7] Aharonian, F., et al. 2006, *ApJ*, 636, 777
- [8] Moskalenko, I. V., & Strong, A. W. 1998, *ApJ*, 493, 694
- [9] Vladimirov, A. E., Jóhannesson, G., Moskalenko, I. V., & Porter, T. A. 2012, *ApJ*, 752, 68
- [10] Damiani, F., Maggio, A., Micela, G., & Sciortino, S. 1997, *ApJ*, 483, 350
- [11] Ciprini, S., et al. 2007, in *American Institute of Physics Conference Series*, Vol. 921, *The First GLAST Symposium*, ed. S. Ritz, P. Michelson, & C. A. Meegan, 546–547
- [12] Ackermann, M., et al. 2012, *ApJ*, 750, 3
- [13] Wolleben, M. 2007, *ApJ*, 664, 349
- [14] Acero, F., et al. 2015, *ApJS*, 218, 23
- [15] Yusifov, I., & Küçük, I. 2004, *A&A*, 422, 545
- [16] Bronfman, L., Casassus, S., May, J., & Nyman, L.-Å. 2000, *A&A*, 358, 521
- [17] Górski, K. M., et al. 2005, *ApJ*, 622, 759
- [18] Kerr, M. 2011, *ArXiv e-prints*
- [19] Lande, J., et al. 2012, *ApJ*, 756, 5
- [20] Abdo, A. A., et al. 2010, *ApJ*, 718, 348
- [21] Green, D. A. 2014, *Bulletin of the Astronomical Society of India*, 42, 47
- [22] Manchester, R. N., Hobbs, G. B., Teoh, A., & Hobbs, M. 2005, *Astron. J.*, 129, 1993
- [23] Navarro, J. F., Frenk, C. S., & White, S. D. M. 1997, *ApJ*, 490, 493